Applied Physics A (2018) 124:34
https://doi.org/10.1007/s00339-017-1441-0

Applied Physics A
Materials Science & Processing

Structural and electrochemical analysis of chemically synthesized microcubic architectured lead selenide thin films

T. S. Bhat[1] · A. V. Shinde[1] · R. S. Devan[2] · A. M. Teli[1] · Y. R. Ma[3] · J. H. Kim[4] · P. S. Patil[1]

Received: 3 October 2017 / Accepted: 29 November 2017

Abstract
The present work deals with the synthesis of lead selenide (PbSe) thin films by simple and cost-effective chemical bath deposition method with variation in deposition time. The structural, morphological, and electrochemical properties of as-deposited thin films were examined using characterization techniques such as X-ray diffraction spectroscopy (XRD), field-emission scanning electron microscopy (FE-SEM), X-ray photoelectron spectroscopy (XPS), cyclic voltammetry (CV), galvanostatic charge–discharge and electrochemical impedance spectroscopy. XRD reveals formation of rock salt phase cubic structured PbSe. FE-SEM images show the formation of microcubic structured morphology. The existence of the PbSe is confirmed from the XPS analysis. On the other hand, CV curves show four reaction peaks corresponding to oxidation [PbSe and $Pb(OH)_2$] and reduction (PbO_2 and $Pb(OH)_2$) at the surface of PbSe thin films. The PbSe:2 sample deposited for 80 min. shows maximum specific capacitance of 454 ± 5 F g^{-1} obtained at 0.25 mA cm^{-2} current density. The maximum energy density of 69 Wh kg^{-1} was showed by PbSe:2 electrode with a power density of 1077 W kg^{-1}. Furthermore, electrochemical impedance studies of PbSe:2 thin film show 80 ± 3% cycling stability even after 500 CV cycles. Such results show the importance of microcubic structured PbSe thin film as an anode in supercapacitor devices.

1 Introduction

Microstructured material offers invention in the field of superior device fabrication than that of devices with bulk counterparts due to its high surface area and different physico-chemical properties [1–4]. The supercapacitors are being developed for a variety of applications such as mobile electronic devices, back-up power supplies, and hybrid electric vehicles [5–7]. Supercapacitors are mainly divided into two groups according to charge storage mechanism as electrical double layer capacitors (EDLCs) and pseudocapacitors. EDLCs store charges by non-faradic mechanism, while faradic charge mechanism is related to pseudocapacitors [8–10]. Among many electrode materials, RuO_2 shows excellent supercapacitive behavior with high specific capacitance and good reversibility [9]. However, the high cost of ruthenium and problems associated with safety constraints its application as an electrode material. Recently, metal chalcogenide with different microstructures and morphologies have attracted tremendous attention in supercapacitive devices because of their superior electrochemical properties [11, 12].

Various microstructures of PbSe with controlled morphology have been studied extensively [13–16]. PbSe thin films are deposited by various researchers using several methods such as colloidal synthesis [17], chemical vapour deposition [18], successive ionic layer adsorption and reaction [19], atomic layer epitaxy [20], molten salt method [21], etc. The liquid-phase synthesis of PbSe microcrystals mainly consists of hydrothermal method [22], solvothermal method [23], chemical bath deposition method (CBD) [24],

T. S. Bhat and A. V. Shinde have contributed equally to this work.

✉ J. H. Kim
jinhyeok@chonnam.ac.kr

✉ P. S. Patil
psp_phy@unishivaji.ac.in

[1] Thin Film Materials Laboratory, Department of Physics, Shivaji University, Kolhapur, Maharashtra 416 004, India

[2] Discipline of Metallurgy Engineering and Materials Science, Indian Institute of Technology Indore, Khandwa Road, Simrole, Indore 453552, India

[3] Department of Physics, National Dong Hwa University, Hualien 97401, Taiwan, ROC

[4] School of Applied Chemical Engineering, Chonnam National University, Gwangju 500 757, South Korea

Published online: 11 December 2017

etc. Among these methods, CBD has been rank as simple, low-cost process based on increasing saturation of solution for agglomeration of microparticles to form a thin film. It has been found that as temperature increases, a transition occurs from cluster mechanism in the initial stages to ion-by-ion growth for PbSe deposition by CBD which helps in regular, uniform deposition of thin films [23–25]. In the present work, we have prepared PbSe thin films using facile and cost-effective CBD method. The growth mechanism of as-prepared PbSe thin films was studied. The structural, morphological and electrochemical properties of the thin films were studied using various characterization techniques.

2 Experimental details

2.1 Synthesis of PbSe thin films

All the chemicals used in the experiment are of AR grade and used without further purification. PbSe thin films were grown on a polished stainless steel substrate with active area of 1 cm^2 by the CBD method. Lead nitrate [$Pb(NO_3)_2$] and freshly prepared sodium selenosulphate (Na_2SeSO_3) are used as cationic and anionic precursor, respectively. In this work, pH of the cationic precursor was controlled by sodium hydroxide (NaOH). Initially, Na_2SeSO_3 was prepared by a standard procedure mentioned in the previous report [26]. In this experiment, Se metal powder was dissolved in an aqueous solution of sodium sulfite, and the solution was refluxed for 12 h at 70 °C. Unreacted Se was removed by filtration to obtain Se stock solution. 1 M sodium hydroxide was slowly added to an aqueous solution of 0.1 M lead nitrate to maintain pH of the solution at ~ 12, with continuous stirring, the milky white solution obtained at the initial stage becomes clear and transparent at room temperature due to the formation of $Pb(OH)_2$. Then, freshly prepared 0.1 M Na_2SeSO_3 solution was added into the lead nitrate solution and the whole reaction was carried out at 70 °C for 40, 80 and 120 min. and the deposited thin films were abbreviated as PbSe:1, PbSe:2, and PbSe:3, respectively. Furthermore, these films were annealed at 300 °C for 10 min. in an ambient atmosphere.

2.2 Characterization of PbSe thin films

The X-ray diffraction (XRD) pattern was recorded using Rigaku miniflex 600 X-ray diffractometer equipped with Cu radiation (K_α of λ = 1.54 Å). Surface morphology was examined using field-effect scanning electron microscopy (FE-SEM) (JEOL JSM-6500F). The elemental analysis of the film was analyzed using XPS Thermo K-Alpha with the multichannel detector, which has energies from 0.1 to 3 keV. The deposited mass on the substrate was calculated using weight difference method. The electrochemical characterizations were carried out using automatic battery cycler unit (WBCS3000), while electrochemical impedance studies were carried out using AUTOLAB PGSTAT100 FRA 32 potentiostat.

3 Results and discussion

3.1 X-ray diffraction (XRD)

Figure 1 depicts XRD pattern of the PbSe:2 thin-film sample. The most prominent diffraction peak present at 28.7° belongs to (200) showing the major growth of crystallites along [100] direction with presence of weak peaks (111), (220), (311), (222), (400), (331), (420), and (422). This result is well matched with the JCPDS Card no. 02-0588 which confirms the formation of face centered cubic (FCC) structure of PbSe. The sharp and strong diffraction peak confirms the good crystallization of the product. The stainless steel substrate peaks are shown by Δ. No impurity phases were detected in the XRD pattern, confirming the purity of PbSe thin film. The reflections of (200) appear with strong intensity due to the existence of a larger number of (200) planes and growth of microcubes are parallel to the substrate and the (200) facets had more chances to be diffracted [27, 28].

The lattice parameter 'a' for PbSe cubic structure is calculated from the following equation,

$$\frac{1}{d^2} = \frac{h^2 + k^2 + l^2}{a^2}. \quad (1)$$

The average lattice parameter $a = 6.141$ Å is in good agreement with the standard lattice parameters $a = 6.162$ Å. The

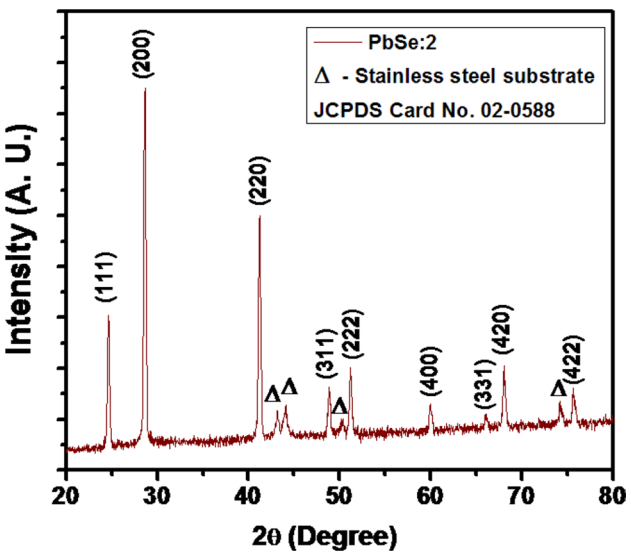

Fig. 1 X-ray diffraction pattern of PbSe:2 thin film

crystallite size calculated from Scherrer formula, was found to be ~35 nm.

3.2 Field-emission scanning electron microscopy (FE-SEM)

Figure 2 shows the FE-SEM images of PbSe:2 sample at different magnifications. The FE-SEM images show the development of merged cube like microarchitectured lead selenide thin film which is compact and uniform throughout the deposited area. Sample shows the formation of denser and compactly arranged structure which is made up of microcubes, as shown in Fig. 2. The average size of microcubes is ~430 nm. It is well known that the crystals are favorable to form a thermodynamically stable structure under right growing conditions. Thus, PbSe cube is having the thermodynamically stable morphology, which can be fast formed in the alkaline medium without additional surfactant [29].

3.3 Growth mechanism

The thin-film deposition is dependent on many factors such as concentration of ions, temperature, pH, and strength of complex formation in the bath, etc. The chemical deposition of metal chalcogenides takes place when its ionic product is greater than the solubility product. In CBD technique, cations and anions slowly release from the precursors, and form nucleation and growth of thin film through the 'ion-by-ion' mechanism. The reaction process for forming lead selenide thin film is considered as follows [30]:

$$Pb(NO_3)_2 + 2NaOH \rightarrow Pb(OH)_2 + 2NaNO_3 \quad (2)$$

$$Pb(OH)_2 + 4NaOH \rightarrow Na_4Pb(OH)_6 \quad (3)$$

$$Na_4Pb(OH)_6 \rightarrow 4Na^+ + HPbO_2^- + 3OH^- + H_2O \quad (4)$$

$$Na_2SeSO_3 + OH^- \rightarrow HSe^- + Na_2SO_4 \quad (5)$$

$$HPbO_2^- + HSe^- \rightarrow PbSe + 2OH^-. \quad (6)$$

Nucleation and growth gives rise to growth of PbSe [31]. In the wet chemical synthesis, tiny seed acts as nucleation center. The shape of seeds is primarily determined by the minimization of surface energy [32]. For an FCC structure, the surface energy (γ) is considered to be in the order $\gamma\{111\} < \gamma\{100\} < \gamma\{110\} < \gamma\{hkl\}$, where {hkl} represents high index facet. The longest direction in a cube is the [111] diagonal according to the lowest energy principle. The ratio of the growth rates in the <100> and <111> direction decides the shape of the nuclei. If the ratio is 0.58, then it forms a perfect cubic shape of the nuclei [33]. The growth rate along the [100] direction is faster than the [111] direction, which induces the shrinking of the six [100] faces into sharp corners and forms cubic shape [34–37]. In this way, different morphologies of the materials are formed by the variation in growth rate of different planes [38]. To minimize the overall surface energy of the system, in this mechanism, the PbSe microparticles gradually evolved into agglomerated cubic shaped structures by dissolve and grow method [39, 40] called as Ostwald ripening effect followed by a non-classical oriented attachment mechanism. Growth occurs at sites where the driving force for crystal is low [41–43]. The screw dislocation plays the role of driving force for the oriented attachment of nuclei particles which result in merging of microcubes appeared in PbSe sample. Under these circumstances, the small cube-shaped structures were formed, as shown in Fig. 2.

3.4 X-ray photoelectron spectroscopy (XPS)

XPS has been used to investigate not only the elemental and chemical composition but also the states of PbSe microcubes. In addition, it examines the oxidation of surfaces. Figure 3a shows the presence of C, O, Pb, and Se elements from the typical survey spectrum of the PbSe:2 sample.

High-resolution XPS spectra for the elements Pb and Se are shown in Fig. 3b, c, respectively. Figure 3b shows the doublets features of the Pb (4f) spectrum, i.e., Pb ($4f_{7/2}$) and Pb ($4f_{5/2}$). The results shows the perfect fit

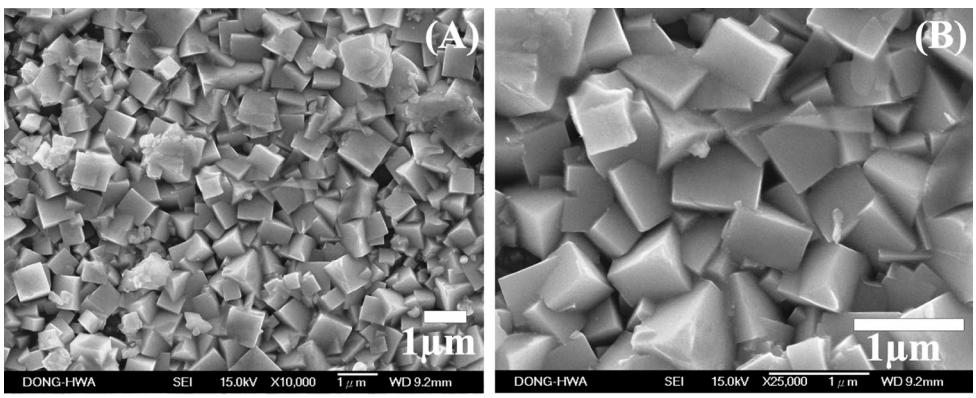

Fig. 2 FE-SEM images show interlocked micro-cubes like morphology of PbSe:2 sample synthesized by chemical bath deposition at **a** ×5000, **b** ×25,000 magnifications

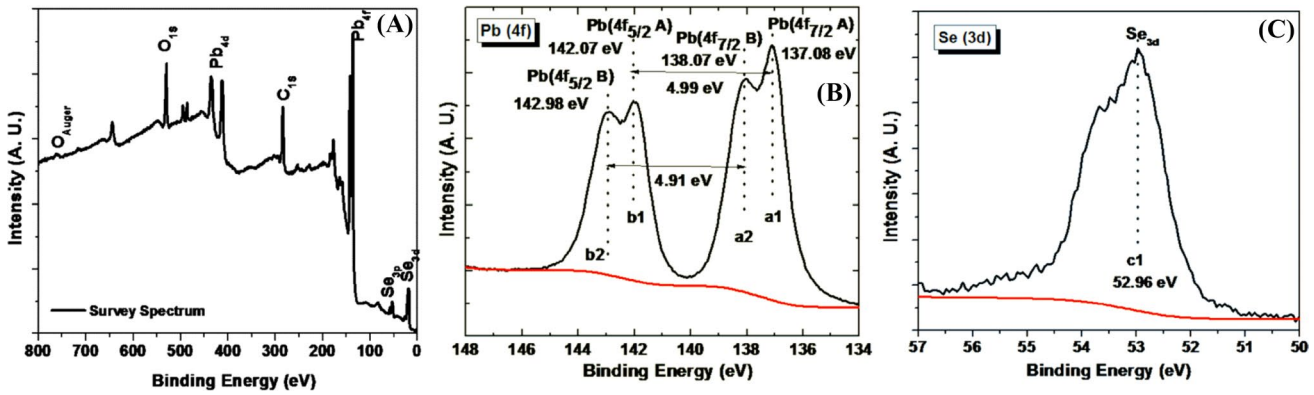

Fig. 3 X-ray photoelectron spectroscopy (XPS) of PbSe microcubes: **a** XPS survey spectrum, **b** high-resolution XPS spectrum of the Pb(4f), and **c** high-resolution XPS spectrum of the Se(3d) level of the PbSe:2 sample

Table 1 Binding energy values of PbSe:2 sample

Sample code	Binding energy (eV)				
PbSe:2	Pb 4f				Se 3d
	Pb $4f_{7/2}$ A	Pb $4f_{7/2}$ B	Pb $4f_{5/2}$ A	Pb $4f_{5/2}$ B	Se $3d_{5/2}$
	137.08	138.07	142.07	142.98	52.96

for the four peaks located at binding energy of 137.08 (Pb ($4f_{7/2}$ A)), 138.07 (Pb ($4f_{7/2}$ B)), 142.07 (Pb ($4f_{5/2}$ A)), and 142.98 (Pb ($4f_{5/2}$ B)) for the double peak features of Pb (4f). Amongst them, highly intense peaks of binding energy 137.08 and 142.07 eV correspond to the (Pb ($4f_{7/2}$ A)) and (Pb ($4f_{5/2}$ A)) core levels of the Pb^{2+} cations, respectively. The peaks located at a binding energy of 138.07 (Pb ($4f_{7/2}$ B)) and 142.98 (Pb ($4f_{5/2}$ B)), respectively, correspond to the core levels of the Pb^{2+} cations of PbO [44, 45]. Moreover, less intensity of these peaks clearly indicates presence of very small amount of PbO along with PbSe. The Se (3d) XPS spectra of the PbSe:2 thin film shown in Fig. 3c denotes peak located at 52.96 eV which corresponds to the Se($3d_{5/2}$) core level of Se^{2-} of PbSe. The energy separation of 4.85 eV between core levels of Pb (4f) reflects a strong binding between the Pb atoms [46–48].

Figure 3a shows the O (1 s) peak from PbSe:2 thin film confirm that the O (1 s) is associated with the Pb–O chemical binding forms lead oxide due to the surface contamination like oxide and hydroxides [49]. The values of binding energy with corresponding peak positions are shown in Table 1. Overall XPS study proves that the synthesized PbSe:2 sample is composed of PbSe along with a minor traces of PbO.

3.5 Electrochemical characterizations

Electrochemical measurements of the PbSe thin films were examined by three electrode system. Here, PbSe thin films are used as working electrode, the counter electrode is platinum substrate, while saturated calomel electrode stands as a reference electrode. All the electrochemical measurements were taken in 1 M NaOH electrolyte at room temperature.

Cyclic voltammetry (CV) is an important tool to study the electrochemical properties of various materials. In CV, one can promptly activate material by delivering electrons and predict the reaction occurring at a specific voltage from changes recorded in the current. Figure 4a shows CV curves for all three different PbSe samples at scan rate of 20 mV s^{-1}. Table 2 lists the sample codes along with the deposited mass and specific capacitance obtained for PbSe electrodes. Here, PbSe:2 sample shows maximum specific capacitance of 333 F g^{-1} at scan rate 20 mV s^{-1} than other PbSe:1 (211 F g^{-1}) and PbSe:3 (240 F g^{-1}) electrodes. The increased specific capacitance of sample PbSe:2 is due to the uniform microstructure nature of the sample. For the PbSe sample prepared at 120 min., peeling off of active material takes place during the deposition, which leads to decrease in the specific capacitance of PbSe:3 electrode. Hence, PbSe:2 sample is further used for detailed electrochemical study. CV curves are incorporated with various oxidation and reduction peaks. The two oxidation peaks at −0.5 and −0.63 V (for PbSe:2) represent oxidation of PbSe and $Pb(OH)_2$, while peaks at −0.67 and −0.92 V are due to the reduction of PbO_2 and $Pb(OH)_2$, respectively [50, 51]. For CV measurements, we have to optimize electrochemical potential window. It is the voltage range between oxidation and reduction potential of given material. The higher potential may damage the material and will reduce cyclic lifetime. To optimize suitable potential window for electrochemical measurements, CV cycles were repeated over a potential window from 0 to −0.8, −1.2 V as shown in

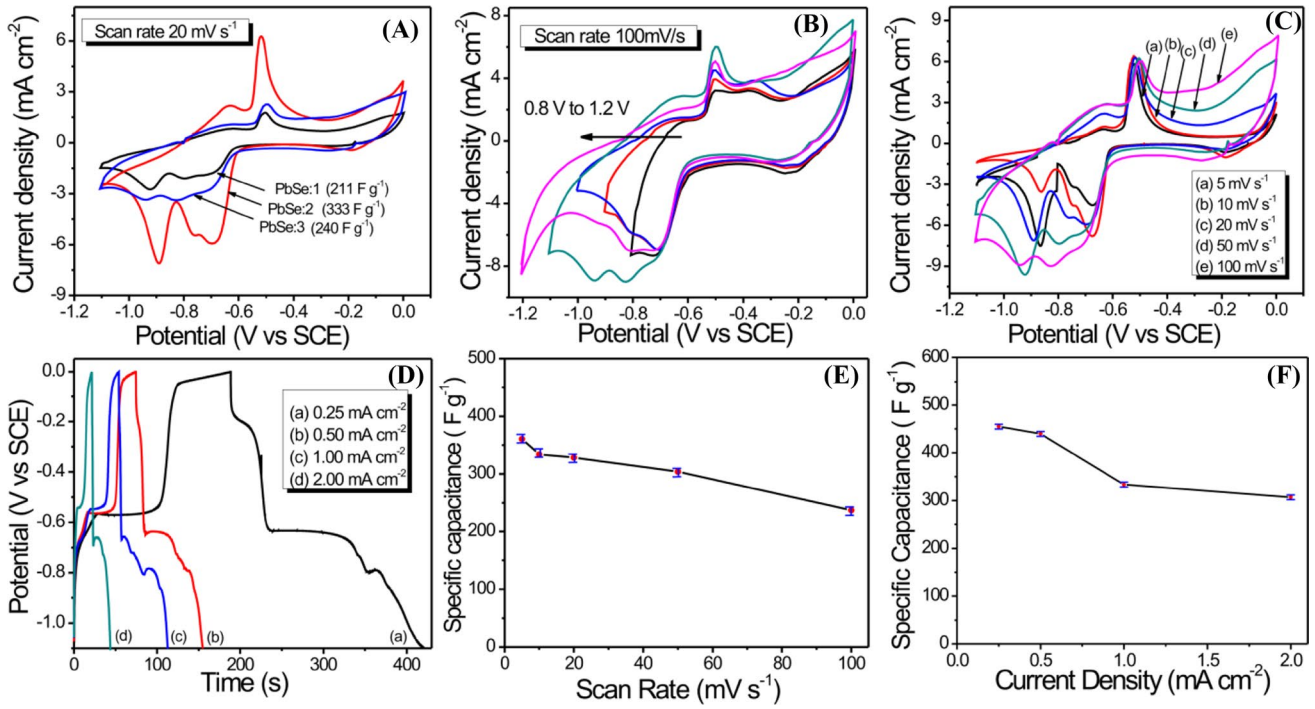

Fig. 4 **a** CV curve of PbSe:1, PbSe:2, and PbSe:3 electrodes at scan rate of 20 mV s^{-1}. **b** Window variation (0–1.2 V) at scan rate of 100 mV s^{-1} for PbSe:2 electrode, **c** CV curves at various scan rate for PbSe:2 electrode, **d** GCD curves at various current densities, **e** Graph of specific capacitance as a function of scan rate with error of ±5 F g^{-1}, **f** Graph of specific capacitance as a function of current densities with error of ±5 F g^{-1} for PbSe:2 electrode

Table 2 Sample code, deposited weight, and specific capacitance measured at 20 mV/s for all PbSe samples

Sr. no.	Sample code	Deposited weight (g)	Specific capacitance (F g^{-1})
1	PbSe:1	0.0008	211
2	PbSe:2	0.0012	333
3	PbSe:3	0.0007	240

Fig. 4b. The area under the CV curve increases simultaneously with an increase in the potential window at a scan rate of 100 mV s^{-1} upto 1.1 V. The potential window of 0–1.2 V shows a drastic change in current with respect to the voltage at a reverse sweep. Hence, potential window of 0–1.1 V is selected for further measurements. It is desirable to revel that the peak is due to oxidation of PbSe which is dwarf due to its insolubility [52]. Figure 4c shows variation in CV curves as a function of scan rate. As scan rate decreases, the area under the curves shrinks with oxidation peaks shift to the left, while reduction peaks shift to the right. This may be attributed as, at higher scan rate, the rate of reaction is larger than at lower scan rate. Figure 4d shows the galvanostatic charge–discharge (GCD) study of PbSe:2 electrode at different current densities ranging from 0.25 to 2 mA cm^{-2}. It is easily seen that GCD curves can be divided into two processes as rapid potential drop and then followed by slow potential decay. Former represents internal resistance, while later shows the capacitive behavior of electrode [50–52]. Specific capacitance (C_{sp}) was calculated from both CV and GCD curves. The C_{sp} value of the PbSe electrode by CV study can be computed by integrating the area under of CV and then dividing by the scan rate (v), the mass of the deposited material (m) in the electrode, and the potential window ($V_a - V_c$) according to the following equation.

$$C_{sp} = \frac{1}{mv(V_c - V_a)} \int_{V_a}^{V_c} I(V)\mathrm{d}V. \quad (7)$$

Figure 4e shows specific capacitance as a function of scan rate. Maximum C_{sp} of 360 F g^{-1} was obtained at a scan rate of 5 mV s^{-1} which further decline upto 273 F g^{-1} at 100 mV s^{-1}. Only 24% of fading in C_{sp} is observed over increasing scan rate from 5 to 100 mV s^{-1} with error of ±5 F g^{-1}. This result shows that microcubic morphology of PbSe:2 electrode helps in ion diffusion process which increases C_{sp} even at the higher scan rate. In addition, the C_{sp} value can be alternatively computed from the discharge curve according to the equation:

$$C_{sp} = \frac{I_d \times T_d}{\Delta V \times m}, \tag{8}$$

where C_{sp} is specific capacitance, I_d is discharged current, T_d is the discharge time, ΔV is working potential window, and m is the mass of deposited material. Figure 4f shows that maximum C_{sp} of 454 F g^{-1} with error of ±5 F g^{-1} is obtained at current density of 0.25 mA cm^{-2} which reduces to 306 F g^{-1} at 2 mA cm^{-2} with only 32% fading at higher current density for PbSe:2 electrode. Such decrement in C_{sp} may be due to time constraint in the motion of charges to cover electrode area.

Ragone plot is further used to relate energy densities (ED) and power densities (PD) to examine the performance of PbSe:2 electrode. The ED and PD values were calculated by the following equations:

$$\text{ED} = \frac{0.5 \times C_s \times \left(V_{max}^2 - V_{min}^2\right)}{3.6} \tag{9}$$

$$\text{PD} = \frac{E \times 3600}{T_d}. \tag{10}$$

Figure 5a shows that the PbSe:2 electrode delivers high ED of 69 Wh kg^{-1} at a power density of 1077 W kg^{-1} and still maintains 46 Wh kg^{-1} at higher 7670 W kg^{-1}. Furthermore, the cell is analyzed by using EIS. Figure 5b shows a Nyquist plot of PbSe:2 sample. It is characterized by equivalent series resistance (ESR) and charges transfer resistance (R_{ct}). ESR consists of solution resistance, the intrinsic resistance of the electrode material, and the contact resistance of an active material to the current collector, while R_{ct} includes the internal resistance of electrodes and double layer capacitance [53]. The Nyquist plot shows semicircle at high frequency followed by a straight line at a lower frequency. The intercept of the semicircle to real axis gives ESR, while R_{ct} is given by diameter of the semicircle. An experimental result shows ESR of PbSe:2 thin film is 0.04 Ω cm^{-2}, while R_{ct} is 3.93 Ω cm^{-2}. Figure 5c gives equivalent electrical circuit for electrochemical cell set up. Electrochemical stability is another crucial factor which contradicts practical application of electrode materials. Figure 5d shows a graph of the area under CV curve retain as a function of CV cycle number. Inset of Fig. 5d shows CV curve at different cycles. PbSe:2 electrode shows almost 80 ± 3% of area retention after 500 cycles which make it promising electrode material for supercapacitive devices.

4 Conclusions

In conclusion, cubic microstructured PbSe thin films were deposited on stainless steel substrate by simple and cost-effective CBD method. The growth mechanism of PbSe

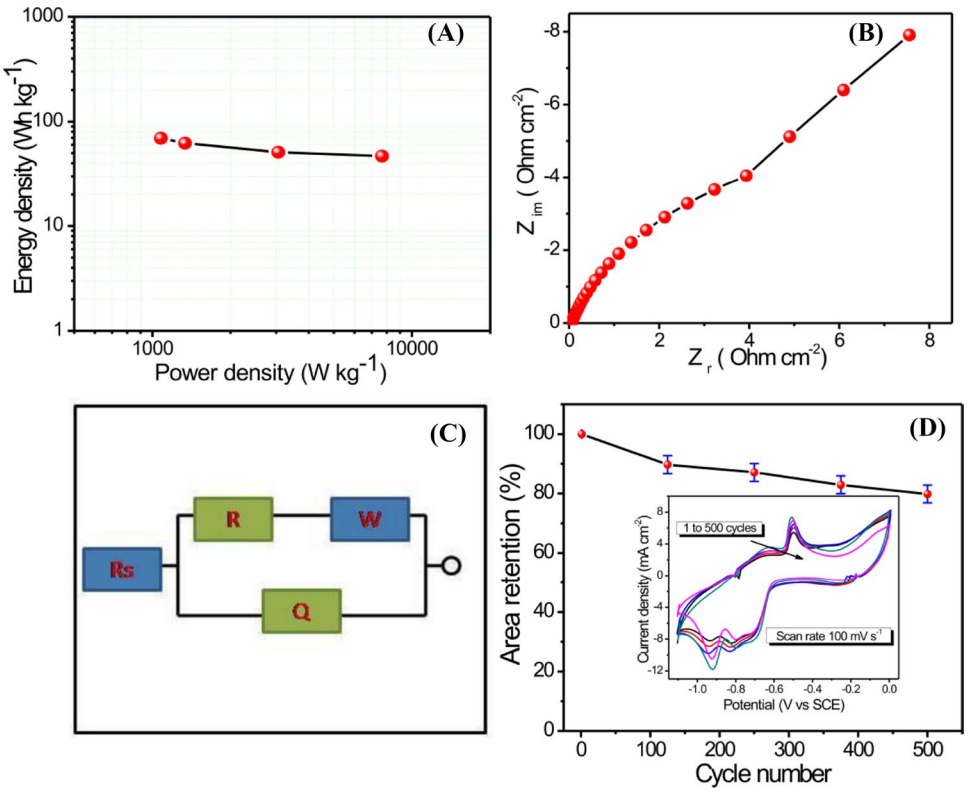

Fig. 5 **a** Ragone plot, **b** Nyquist plot, **c** equivalent circuit, and **d** graph of capacity retention as a function of cycle numbers with error of ±3% (inset shows CV curves at various cycle number) for PbSe:2 electrode

thin films is studied. The XRD ad XPS analysis confirms the PbSe formation. The FE-SEM images show uniform, merged microcubes like morphologies. In electrochemical characterization, CV curves show four reaction peaks corresponding to oxidation of the PbSe and $Pb(OH)_2$, and reduction of PbO_2 and $Pb(OH)_2$. From the galvanostatic charge–discharge study, maximum C_{sp} of 454 ± 5 F g^{-1} is achieved at 0.25 mA cm^{-2} current density with energy density of 69 Wh kg^{-1} at higher power density 1077 W kg^{-1} for PbSe:2 sample. Nearly $80 \pm 3\%$ of cycling stability is shown by PbSe:2 electrode at posterior of 500 CV cycles. By virtue of these attributes, we can conclude that PbSe thin films are a promising material for the development of high-performance supercapacitors.

Acknowledgements One of the author TSB is thankful to the University Grants Commission (UGC) New Delhi, India for awarding the UGC-BSR (JRF) fellowship (Grant no. F.25-1/2013-14(BSR)/7-167/2007 (BSR)) for financial support. Author AVS is thankful to the Department of Science and Technology (DST) New Delhi, India for awarding 'Scholarship for Higher Education (SHE) (2205/2012)' through 'INSPIRE' scheme. This work is supported by University Grants Commission (UGC), New Delhi, through the project no. 43-517/2014(SR) and partially supported by the Human Resources Development program (no.: 20124010203180) of the Korea Institute of Energy Technology Evaluation and Planning (KETEP) grant funded by the Korea government Ministry of Trade, Industry, and Energy.

References

1. K. Ardakania, M. Holl, Prog. Mater. Sci. **87**, 221 (2017)
2. C. Hou, M. Zhang, A. Halder, Q. Chi, Electrochim. Acta **242**, 202 (2017)
3. K. Pathakoti, M. Manubolu, H. Hwang, J. Food Drug Anal. **25**, 245 (2017)
4. P. Lund, Microelectron. Eng. **108**, 84 (2013)
5. S. Sarangapani, B.V. Tilak, C.P. Chen, J. Electrochem. Soc. **143**, 3791 (1996)
6. B.E. Conway, *Electrochemical Supercapacitors* (Kluwer Academic/Plenum Publishers, New York, 1999)
7. C. Subramanian, H. Zhu, R. Vajtai, P.M. Ajayan, B. Wei, J. Phys. Chem. B **109**, 20207 (2005)
8. Q. Tang, M. Chen, L. Wang, G. Wang, J. Power Sources **273**, 654 (2015)
9. A. Shinde, N. Chodankar, V. Lokhande, A. Lokhande, T. Ji, J. Kim, C. Lokhande, RSC Adv. **6**, 58839 (2016)
10. W. Wang, S. Guo, I. Lee, K. Ahmed, J. Zhong, Z. Favors, F. Zaera, M. Ozkan, C. Ozkan, Sci. Rep. **4**, 4452 (2014)
11. W. Liao, B. Wang, Z. Liu, Int. J. Hydrog. Energy **42**, 10962 (2017)
12. L. Zhang, B. Zhang, L. Ning, S. Li, Y. Zheng, Opt. Commun. **383**, 371 (2017)
13. S. Lee, Y. Wang, Y. Liu, D. Lee, K. Lee, D. Lee, T. Lian, Chem. Phys. Lett. **683**, 342 (2017)
14. Y. Suh, S. Suh, S. Lee, G. Kim, Thin Solid Films **628**, 148 (2017)
15. W. Feng, X. Wang, F. Chen, W. Liu, H. Zhou, S. Wang, H. Li, Thin Solid Films **578**, 25 (2015)
16. E. Torresa, M. López, Y. Matsumoto, J. Salazarc, Mater. Res. Bull. **80**, 96 (2016)
17. B. Wagner, N. Singh, S. McLaughlin, A. Berghmans, D. Kahler, D. Knuteson, J. Cryst. Growth **311**, 1080 (2009)
18. D. Talapin, H. Yu, E. Shevchenko, A. Lobo, C. Murray, J. Phys. Chem. C **111**, 14049 (2007)
19. T. Bhat, S. Vanalakar, R. Devan, S. Mali, S. Pawar, Y. Ma, C. Hong, J. Kim, P. Patil, J. Mater. Sci. Mater. Electron. **27**, 4996 (2016)
20. I. Urbiola, J. Martínez, J. Borja, C. García, R. Bon, Y. Vorobiev, Energy Proc. **57**, 24 (2014)
21. A. Osherov, M. Shandalov, V. Ezersky, Y. Golan, J. Cryst. Growth **304**, 169 (2007)
22. L. Jin, Z. Yabo, Y. Dagen, H. Zhanjun, J. Cryst. Growth **304**, 169 (2007)
23. E. El-Menyawy, G. Mahmoud, S. Gad, A. Azab, F. Terr, J. Inorg. Organomet. Polym. Mater. **25**, 1044 (2015)
24. C. Zhang, Z. Kang, E. Shen, E. Wang, L. Gao, F. Luo, C. Tian, C. Wang, Y. Lan, J. Phys. Chem. B **110**, 184 (2006)
25. P. Isi, P. Ekwo, Res. J. Eng. Sci **2**, 15 (2013)
26. S. Gorer, G. Hodes, J. Phys. Chem. **98**, 5338 (1994)
27. Y. Lau, D. Chernak, M. Bierman, S. Jin, J. Mater. Chem. **19**, 934 (2009)
28. R. Perez, G. Tellez, U. Rosas, A. Torres, J. Tecorralco, L. Lima, O. Moreno, Mater. Sci. Eng. A **3**, 1 (2013)
29. J. Cui, F. Guo, X. Liu, Chem. Lett. **34**, 170 (2005)
30. S. Mahmoud, O. Hamid, FIZIKA A (Zagreb) **10**, 21 (2001)
31. W. Burton, N. Cabrera, F. Frank, Nature **163**, 398 (1949)
32. Y. Xiong, Y. Xia, Adv. Mater. **19**, 3385 (2003)
33. Z. Wang, J. Phys. Chem. B **104**, 1153 (2000)
34. I. Pintilie, E. Pentia, L. Pintilie, D. Petre, C. Constantin, T. Botila, J. Appl. Phys. **78**, 1713 (1995)
35. C. Li, T. Bai, F. Li, L. Wang, X. Wu, L. Yuan, Z. Shi, S. Feng, Cryst. Eng. Commun. **15**, 597 (2013)
36. J. Petroski, Z. Wang, T. Green, M. Sayed, J. Phys. Chem. B **102**, 3316 (1998)
37. H. abrisch, L. Kjeldgaard, E. Johnson, U. Dahmen, Acta Mater. **49**, 4259 (2001)
38. Y. Tang, W. Cheng, Nanoscale **7**, 16151 (2015)
39. G. Xi, J. Ye, Inorg. Chem. **49**, 2302 (2010)
40. S. Lee, S. Cho, J. Cheon, Adv. Mater. **15**, 441 (2003)
41. S. Amelinckx, Philos. Mag. **44**, 337 (1953)
42. R. Penn, J. Banfield, Science **281**, 969 (1998)
43. Q. Wang, G. Chen, H. Yin, J. Mater. Chem. A **1**, 15355 (2013)
44. R. Trujillo, E. Rosendo, M. Ortega, A. Sanchez, J. Gracia, T. Dıaz, G. Nieto, G. Garcıa, J. Lopez, M. Pacio, Nanotechnology **23**, 185602 (2012)
45. S. Mali, S. Desai, S. Kalagi, C. Betty, P. Bhosale, R. Devan, Y. Ma, P. Patil, Dalton Trans. **41**, 6130 (2012)
46. J. Zhu, H. Wang, S. Xu, H. Chen, Langmuir **18**, 3306 (2002)
47. J. Moulder, W. Stickle, P. Sobol, K. Bomben, *Handbook of X-ray Photoelectron Spectroscopy* (Perkin-Elmer Corp, Eden Prairie, 1992), pp. 92–93
48. S. Pawar, R. Devan, D. Patil, A. Moholkar, M. Gang, Y. Ma, J. Kim, P. Patil, Electrochim. Acta **98**, 244 (2013)
49. R. Devan, C. Lin, S. Gao, C. Cheng, Y. Liou, Y. Ma, Phys. Chem. Chem. Phys. **13**, 13441 (2011)
50. J. Xie, F. Tu, Q. Suc, G. Du, S. Zhang, T. Zhu, G. Cao, X. Zhao, Nano Energy **5**, 122 (2014)
51. E. Gobert, O. Vittoki, Electrichim. Acta **33**, 245 (1998)
52. X. Chen, Y. Zhu, Z. Xing, G. Tang, H. Fan, J. Mater. Sci. Mater. Electron. **27**, 1155 (2016)
53. N. Chodankar, G. Gund, D. Dubal, C. Lokhande, RSC Adv. **4**, 61503 (2014)